ELSEVIER

# Fabrication and characterization of microfluidic probes for convection enhanced drug delivery

K.B. Neeves [a], C.T. Lo [b], C.P. Foley [a], W.M. Saltzman [b], W.L. Olbricht [a,*]

[a] *School of Chemical and Biomolecular Engineering, Cornell University, Ithaca, NY 14853, USA*
[b] *Department of Biomedical Engineering, Yale University, New Haven, CT 06520, USA*

## Abstract

Convection enhanced drug delivery (CED) is a promising therapeutic method for treating diseases of the brain by enhancing the penetration of drugs. Most controlled release delivery methods rely on diffusion from a source to transport drugs throughout tissue. CED relies on direct infusion of drugs into tissue at a sufficiently high rate so that convective transport of drug is at least as important as diffusive transport. This work describes the fabrication and characterization of microfluidic probes for CED protocols and the role diffusion plays in determining penetration. Microfluidic channels were formed on silicon substrates by employing a sacrificial photoresist layer encased in a parylene structural layer. Flow in the microchannels was characterized by applying constant upstream pressures from 35 to 310 kPa, which resulted in flow rates of 0.5–4.5 μL/min. The devices were used to infuse Evans Blue and albumin in hydrogel brain phantoms. The results of these infusions were compared to a simple convection–diffusion model for infusions into porous media. In vivo infusions of albumin were performed in the gray matter of rats at upstream pressures of 35, 70, and 140 kPa. The microfabricated probes show reduced evidence of backflow along the device–tissue interface when compared with conventional needles used for CED.
© 2005 Elsevier B.V. All rights reserved.

## 1. Introduction

Numerous localized drug delivery strategies have been developed to circumvent the blood brain barrier. For example, the insertion of polymeric implants that release drugs slowly into the surrounding tissue has been successful in treating tissues locally [1]. These implants also can be effective in treating intracranial tumors with local chemotherapy because high drug doses can be delivered to the tissue surrounding the implant [2]. However, the distance that a drug penetrates into the tissue after release depends on the relative rates of drug transport and drug elimination [3]. When diffusion is the dominant transport mechanism, the concentration of the drug decays exponentially with distance from the implant. In many instances, only the tissue within a few millimeters of the implant is exposed to a therapeutically useful drug concentration. In this case, treatment could be enhanced by alternative delivery methods that increase the penetration distance of the drug into tissue and eliminate the rapid decay in concentration with distance that is characteristic of diffusion mediated transport.

Convection-enhanced drug delivery (CED) uses direct infusion of a drug-containing liquid into tissue so that transport is dominated by convection. By increasing the rate of infusion, the convection rate can be made large compared with the elimination rate in a region of tissue about the infusion point. Thus, CED has the potential of increasing the drug penetration distance and mitigating the decay in concentration with distance from the release point. In addition, CED may overcome limitations of traditional treatments for brain tumors caused by the large tumor size and the difficulty of delivering therapeutics into their dense tissue.

Convection-enhanced drug delivery has been tested extensively in animals and humans. Small molecules [4–6], proteins [7–9], growth factors [10,11], and nucleotides [12,13] have

* Corresponding author. Tel.: +1 607 255 9491; fax: +1 607 255 9166.
*E-mail address:* wlo1@cornell.edu (W.L. Olbricht).

been infused into animal models for therapeutic and imaging purposes. Chemotherapy agents [14,15], viral vectors [16], and proteins [17,18] have been infused into humans in clinical trials. Initial studies were confined to infusion in the homogenous, gray matter bodies of the brain [7,12]. Other studies have concentrated on the globus pallidus internus [5], peripheral nerves [19], tumors [11,14], and the brainstem [20,9,21]. The results of these studies indicate that convection can be used to distribute molecules, regardless of their size, throughout most regions of the brain. However, it can be difficult to control the distribution of infused molecules when characteristics of the tissue vary within the treatment region, such as in heterogenous tumors [22] and near white matter tracts in the brain [23]. Clinical trials for treating brain tumors have reported similar problems in tracking and predicting the distribution of infused chemotherapy agents [24].

CED involves inserting a small cannula or needle into an afflicted area and infusing drug or imaging solutions at a specified flow rate. This cannula is most often a stainless steel needle ranging from 20 to 32 ga in size. In prior studies flow rates ranged from 0.1 to 10 μL/min and were controlled with an external syringe pump. At flow rates greater than 1 μL/min, backflow of infused solutions up the outside of the needle shaft has been reported [25]. Apparently, at sufficiently high flow rates, the tissue separates from the needle, and injected fluid flows preferentially along the separation. Backflow reduces control over drug delivery because infused solutions can flow out of the brain or into highly permeable white matter tracts surrounding the infusion site. The separation that allows backflow can be controlled by adjusting the flow rate and the size of the needle [26].

Another problem encountered with needles is an unexpectedly large pressure at the needle tip at the start of an infusion. The large pressure may indicate that the tip of the needle is partially or fully occluded when it is inserted into the brain. It has been suggested that a needle or catheter with fluid outlets along its side, rather than at its tip, could alleviate some of these problems [27].

Microfabricated devices offer several potential advantages over needles and catheters for CED. A microfabricated device could be made small to minimize tissue damage [28], reduce backflow, yet rigid enough to penetrate deep into tissue. The fluid outlet could be located away from the penetrating edge of the device to avoid occlusion of the channel. Furthermore, microfabrication offers the possibility of integrating electrical, mechanical, and chemical sensors with the fluid delivery system [29,30,28]. For example, microfluidics have been added to silicon microelectrodes to control the local chemical environment during extracellular recordings in the cortex [31]. Microneedles with on-chip flow meters [32] and pumps [33] provide fluid flow control and minimize reagent volume. The implantation of silicon devices has been extensively characterized for cortical neural prosthetics [34]. Some implanted devices have recorded electrical signals for up to one year in vivo [35]. Other neuroscience applications for which microfluidic devices may be useful include measuring cerebrospinal fluid flow [36], infusing neurotransmitters and

neurotrophic factors [37,38], and studying addiction mechanisms [39].

A first step in building an integrated microfluidic delivery system for CED is to demonstrate that fluid can be delivered through a microfabricated device at rates comparable to those for needles and cannulas. This study describes the microfabrication and testing of a device that can be inserted into brain tissue and deliver flow rates appropriate for CED (0.1–5 μL/min). The device is designed to deliver fluid to the caudate nucleus of adult rats for direct comparison with previous studies that used needles [7,25,26]. Infusions into agarose brain phantoms and the rat caudate are examined to determine whether higher flow rates can be achieved, without significant fluid reflux, with microfluidic devices than with standard needles. In addition, an analytical model is developed to examine the effect of diffusion on the penetration of infused drugs.

## 2. Methods and materials

### 2.1. Fabrication of microfluidic probes

Devices were fabricated using standard micromachining techniques for patterning silicon and polymer layers. Fig. 1 shows a schematic of the fabrication process, which involves a series of patterning, deposition, and removal steps. The finished device consists of three parts shown in Fig. 2: an insertable microprobe with a cross-section of $100 \times 100$ μm and a length that varies from 2 to 5 mm, a square handle with dimensions of 2 mm × 2 mm × 300 μm, and a protrusion with a length of 2 mm and a cross-section of $100 \times 100$ μm that can be connected to external tubing.

To start the fabrication a silicon dioxide etch mask was deposited on the backside of a double-sided, polished silicon wafer with a thickness of 300 μm (Fig. 1(a)). The backside of the wafer was then etched with deep reactive ion etching to a depth of 200 μm to define the insert and protrusion thickness (Fig. 1(b)). A 2 μm silicon dioxide layer was then deposited on the backside of the wafer using plasma enhanced chemical vapor deposition (PECVD). This layer acts as an etch stop when the front side of the wafer is etched in a subsequent step (Fig. 1(c)).

To form a base layer for the microchannel, a 5 μm thick layer of positive tone polyimide (Photoneece, Toray Industries, Japan) was spun, patterned, and cured on the front side of the wafer (Fig. 1(d)). Next, sacrificial photoresist was spun on top of the polyimide to form a layer of height 10–15 μm. The wafer was then soft-baked in a convection oven at 90 °C for 30 min. The photoresist was patterned and developed, leaving photoresist in place to define the microchannel (Fig. 1(e)). The assembly was hard-baked at 90 °C for 5 min. The polyimide base layer was then roughened with an oxygen plasma (400 W, 1 min) to promote adhesion between polyimide and parylene. A layer of parylene C (Specialty Coating Systems) was then deposited to a thickness of 5 μm (Fig. 1(f)).

Following parylene deposition, a 100 nm layer of aluminum was electron beam evaporated and patterned in the shape of the
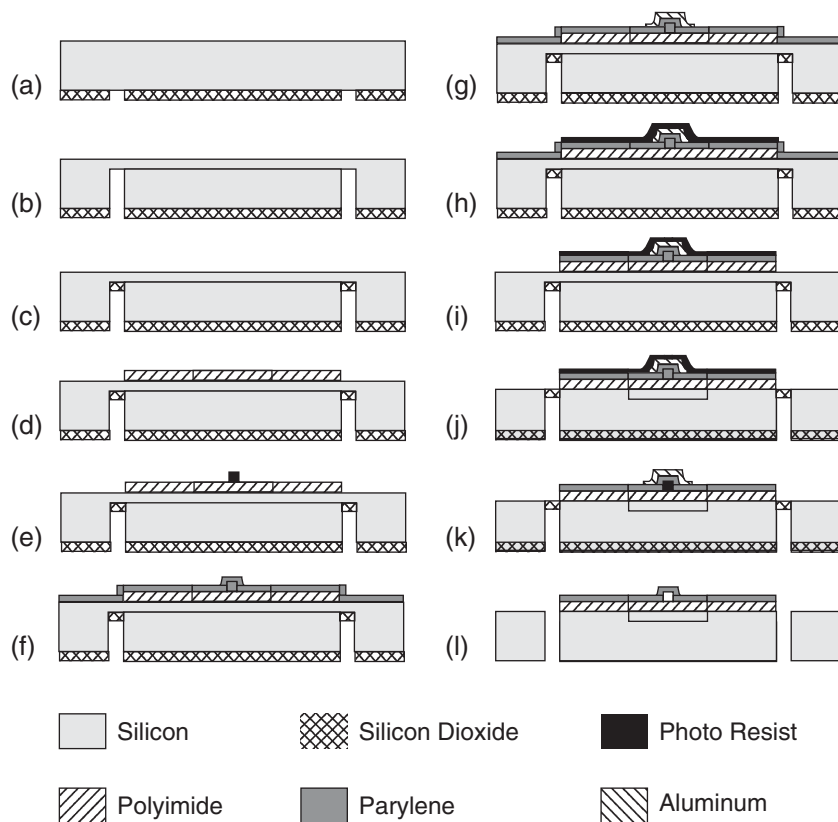
Fig. 1. Summary of fabrication process; a) Deposition and patterning of silicon dioxide etch mask, b) DRIE of backside silicon, c) Deposition of silicon dioxide etch stop, d) Patterning of photosensitive polyimide adhesion layer, e) Patterning of sacrificial photoresist layer, f) Deposition parylene structural layer, g) Evaporation and patterning of aluminum etch mask, h) Patterning of photoresist etch mask, i) Patterning of parylene by oxygen plasma, j) DRIE of front side silicon, k) Definition of channel inlet and outlet in parylene by oxygen plasma, l) Dissolution of silicon oxide and aluminum in buffered oxide etch and release of sacrificial photoresist in acetone.

channels (Fig. 1(g)). The aluminum acts as a mask for etching the inlet and outlet holes of the channel. A subsequent resist layer was spun and patterned to serve as an etch mask for both the bulk parylene etch and the silicon deep reactive ion etch (Fig. 1(h)). Parylene was etched with 150 W oxygen plasma at a rate of 100 nm/min (Fig. 1(i)). The silicon was etched down to the oxide etch stop to define the insert and protrusion geometry (Fig. 1(j)). Next, the inlet and outlet holes were etched in the parylene layer using the aluminum etch mask (Fig. 1(k)). The oxide etch stop and aluminum mask were simultaneously removed in buffered oxide etch. Finally, the photoresist was removed from the channels in an acetone bath for 4 h followed by 4 h in isopropyl alcohol and 12 h in deionized water (Fig. 1(l)).

This procedure can be used to fabricate channels with heights between 1 and 20 μm and widths between 10 and 100 μm. The channels used in this study had a height of 10 μm and a width of 50 μm. The length of the channel was 8 mm from protrusion to tip.

### 2.2. Experimental set-up

Microfluidic devices were attached to micropipettes (OD = 1 mm, ID = 0.58 mm and OD = 2 mm, ID = 1.12 mm) using two part epoxy. The micropipette was then backfilled with 0.1%

(w/v) Evans Blue, or 1% (w/v) Evans Blue labeled albumin and inserted into a micropipette holder on a micromanipulator. The micropipette holder was connected to a programmable pressure injector (World Precision Instruments PM8000, Sarasota, FL, USA) with low compliance polyethylene tubing. Compressed high purity nitrogen was used as a pressure source. The injector maintained a constant pressure at the inlet of the channel. The flow rate through the devices was determined by measuring the speed of the liquid front in the micropipette. In some experiments a 30 ga blunt needle was used in place of the microfluidic device so that a direct comparison could be made between delivery methods.

Most CED protocols infuse fluid at a constant flow rate, but infusion at constant pressure has distinct advantages here. First, it is easier to manipulate fluid in microfluidic devices by regulating pressure rather than flow rate, especially while priming a channel that is initially filled with air. Second, in constant pressure infusion, the pressure profile in the tissue is independent of tissue material properties (Section 2.6).

### 2.3. Agarose brain phantoms

Agarose gels (0.6% w/v) were used as a brain tissue analog to characterize the delivery from the devices. Flow in agarose at this concentration mimics some characteristics of pressure-
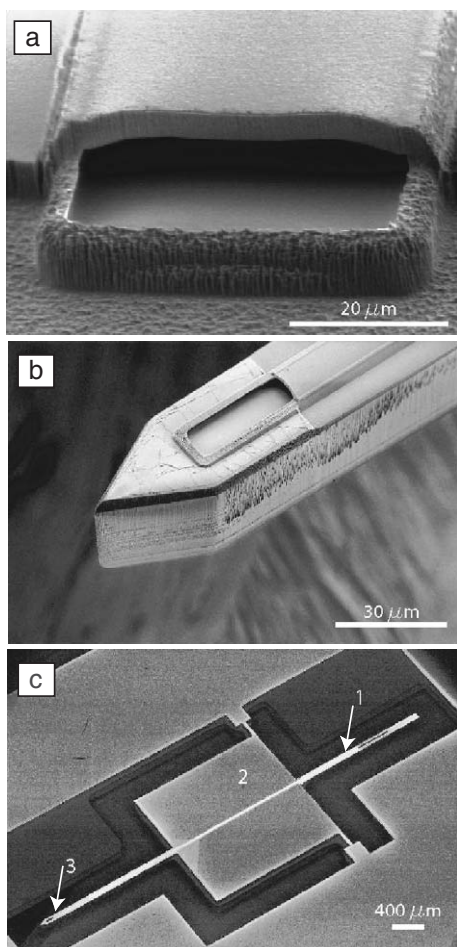
Fig. 2. Electron micrographs of microfluidic probe. (a) Parylene microfluidic channel with dimension of $50 \times 10$ µm. (b) Pointed tip of insertable portion of probe. (c) Entire probe with protrusion for fluidic connection (1), base for handling (2) and tissue penetrating insert (3).

driven flow in brain tissue [27]. Agarose powder was added to Tris–Borate–EDTA (TBE) buffer and heated in a microwave oven on high heat for 90 s while covered. The hot solution was poured into 100 mm tissue culture plates and allowed to gel for 2 h at room temperature. The devices were inserted 5 mm into the gels at a rate of 1 mm/s using a micromanipulator. A fixed volume (ranging from 10 to 40 µL) of the dye solution was infused into the gel at pressures of 35, 70, 140, and 210 kPa. The dye flowed radially outward from the tip of the device and formed an approximately spherical volume about the device tip. After infusion, which lasted between 10 and 80 min, the penetration depth was determined by measuring the diameter of the dyed agarose sphere with calipers.

### 2.4. Animal studies

Twelve male Sprague–Dawley rats (180–200 g) were used to characterize the performance of devices in vivo. Rats were anesthetized with ketamine (100 mg/kg)/xylyzine (10 mg/kg) solution via intraperitoneal injection. The head was shaved and disinfected with butadiene/alcohol/butadiene cotton swabs. An incision was made and a 1 mm diameter hole was drilled in the skull 3 mm laterally from bregma. The device was inserted into the brain at a rate of 1 mm/s with a micromanipulator. The tissue was allowed to equilibrate mechanically for 3 min. Then, a solution Evans Blue labeled albumin was infused at 35, 70, and 140 kPa into the caudate putamen. The flow rate was determined by measuring the fluid speed in the micropipette. After 5 µL of the Evans Blue labeled albumin solution was infused, the device was vented to atmosphere and promptly removed. The animals were immediately sacrificed by carbon dioxide inhalation and the brains were removed and flash frozen in −70 °C hexane. The brains were sectioned into 25 µm slices on a cryostat. Every fifth slice was collected for image analysis. All procedures were done in accordance with the regulations of the Yale University Institutional Animal Care and Use Committee.

### 2.5. Image analysis

Frozen sections of brain tissue sections were imaged using a stereoscope and CCD camera. Images were captured as RGB 8-bit TIFF files using StreamPix software (Norpix Inc., Montreal, Canada). To determine the penetration of the albumin the RGB file was broken into red, green, and blue planes using a Matlab script. Each plane consists of $480 \times 640$ pixels of intensity data on a scale of 0–255. Blue plane pixels were normalized by dividing each individual pixel by the total pixel intensity of all three colors, $B_N = B/(R+G+B)$. A pixel was considered to have a dominant blue intensity if the value of $B_N$ was greater than 0.333. Pixels with values greater than 0.333 were assigned a pixel value of zero, and all pixels with values less than 0.333 were assigned a value of one. The result was binary image where zero is black and one is white. To minimize background noise an erosion operation was applied to each image. The erosion operation specified that if more than four of a black pixel's eight neighbors were white, then that pixel was changed to white. The topology of the thin slices left artifacts in the image that appeared as isolated white pixels within large black, or dyed, areas. A dilation operation was used that specified if more than four of a white pixel's eight neighbors were black, then that pixel was changed to black. After image processing, the area of each slice was calculated by summing the number of black pixels. The *Analyze Particles* tool in ImageJ software (National Institutes of Health, Bethesda, MD) was used to calculate the area of each dye spot and the major and minor axis of an ellipse fit to the spot. Because we were interested in examining drug delivery in gray matter, only dye in the gray matter was considered for calculating the aspect ratio between the major and minor axis.

This method does not measure dye concentration, but instead determines only a threshold concentration. Some of the images from each animal were also imaged by epifluorescence using a rhodamine filter to estimate the threshold concentration. A two-dimensional surface plot of the intensity profile of the fluorescent images was compared to processed stereoscope images. Assuming that intensity is proportional to concentration, the threshold concentration was ~60% of the injected concentration.

## 2.6. Model of fluid transport

Fluid transport during infusion into gels and tissue depends in part on the mechanical response of the medium to the imposed flow. Models have been developed to describe fluid transport in rigid pore [40,41], poroelastic [42,43], and poroviscoelastic [44] models of the medium. Including poroelastic or poroviscoelastic properties in a model is useful for capturing transient responses of the matrix and the time-dependent stress in the matrix. At steady-state, though, the pressure and velocity fields are independent of the particular constitutive assumption for the material. That simplification is exploited here to estimate an apparent hydraulic permeability of the medium and a penetration distance that incorporates the role of diffusion. In the absence of an exact solution of the convective–diffusion equation for this problem, which is beyond the scope of this study, a simplified model is used to estimate the penetration distance of infused compounds [45].

Mass conservation of the tissue solid matrix and fluid constituents can be expressed as

$$\nabla \cdot \left( \phi \boldsymbol{v} + (1-\phi)\frac{\partial \boldsymbol{u}}{\partial t} \right) = 0 \tag{1}$$

where $\boldsymbol{v}$ is the fluid velocity vector, $\boldsymbol{u}$ is the solid matrix velocity vector, and $\phi$ is the porosity. Darcy's law gives the following relationship between velocity and pressure in porous media

$$\phi \left( \boldsymbol{v} - \frac{\partial \boldsymbol{u}}{\partial t} \right) = -\kappa \nabla P \tag{2}$$

where $\kappa$ is the hydraulic permeability and $P$ is the pressure. Assuming steady state and purely radial flow, Eq. (1) becomes

$$\frac{1}{r^2}\frac{\partial}{\partial r}(r^2 \boldsymbol{v}_r) = 0 \tag{3}$$

which is integrated to obtain

$$\boldsymbol{v}_r = \frac{A}{r^2} \tag{4}$$

Substituting Eq. (4) into Eq. (2) and integrating yields

$$P(r) = \frac{\phi}{\kappa}\frac{A}{r} + B \tag{5}$$

The integration constants $A$ and $B$ are found by assuming that the pressure decreases to zero at infinity and that $P(a)=P_o$, where $P_o$ is the pressure inside a fluid-filled cavity of radius $a$ about the tip of the microfluidic channel. Evaluating the constants gives the following pressure and velocity profiles

$$\frac{P(r)}{P_o} = \frac{a}{r} \tag{6}$$

$$\boldsymbol{v}_r(r) = \frac{P_o \kappa a}{\phi r^2} \tag{7}$$

The volumetric flow rate at the channel tip is

$$Q(a) = \phi \boldsymbol{v}_r(a) 4\pi a^2 = 4\pi a \kappa P_o \tag{8}$$

In the experiment, the flow rate, $Q(a)$, is measured for various values of the pressure $P_o$. Eq. (8) suggests that a plot of $Q(a)/4\pi a$ as a function of $P_o$ should give a straight line with a slope that is an apparent permeability of the medium.

The penetration distance of an infused compound can be estimated by assuming that convective and diffusive transport take place in parallel [44]. The characteristic time for diffusion, $\tau_D$ is,

$$\tau_D = \frac{r^2}{D} \tag{9}$$

where $D$ is the diffusion coefficient of the infused molecules in the porous medium. The characteristic time for convection, $\tau_C$ is

$$\tau_C = \int_a^r \frac{\mathrm{d}r'}{\boldsymbol{v}(r')} = \frac{\phi}{3P_o \kappa a}(r^3 - a^3) \tag{10}$$

To estimate the penetration distance after infusion over some time $T$, the inverse characteristic times for diffusion and convection are summed as follows

$$\frac{1}{T} = \frac{1}{\tau_D} + \frac{1}{\tau_C} \tag{11}$$

The value of $r$ that satisfies Eq. (11) is an estimate of the penetration distance $R$.

The Peclet number $Pe = \tau_D / \tau_C$ gives the relative importance of convective transport compared with diffusive transport. For infusion into a porous medium, $Pe$ is a maximum at the infusion point and decreases with distance from the infusion point. In the limit of infinitely large $Pe$, convection dominates fluid transport everywhere and diffusion can be neglected, which yields the convection-dominated penetration distance $R_C$ as a function of time $T$

$$R_C = \left( \frac{3QT}{4\pi\phi} \right)^{1/3} \tag{12}$$

This model is well suited for infusions into gels where there are no elimination mechanisms. The effect of elimination has been treated by Morrison et al. for a rigid pore model [40].

## 3. Results

### 3.1. Device characterization

Constant pressure infusions were controlled by a pressure injector, which sets the pressure upstream of the microchannel to a desired value. However, there is a significant pressure loss over the length of the microchannel, which must be taken into account to find the infusion pressure, $P_o$, at the microchannel exit. To determine this pressure loss as a function of flow rate, flow rates in the microchannel were measured for several injector pressures with the exit of the microchannel outlet immersed in a water reservoir (0 ga pressure). A linear relationship between flow rate and injector pressure was found, which is expected because flow in the microchannel is laminar. The pressure drop $\Delta P$ between the injector and the microchannel exit was found to be $\Delta P$ (in kPa)=70.0 $Q$ (in μL/min). Therefore, during an infusion
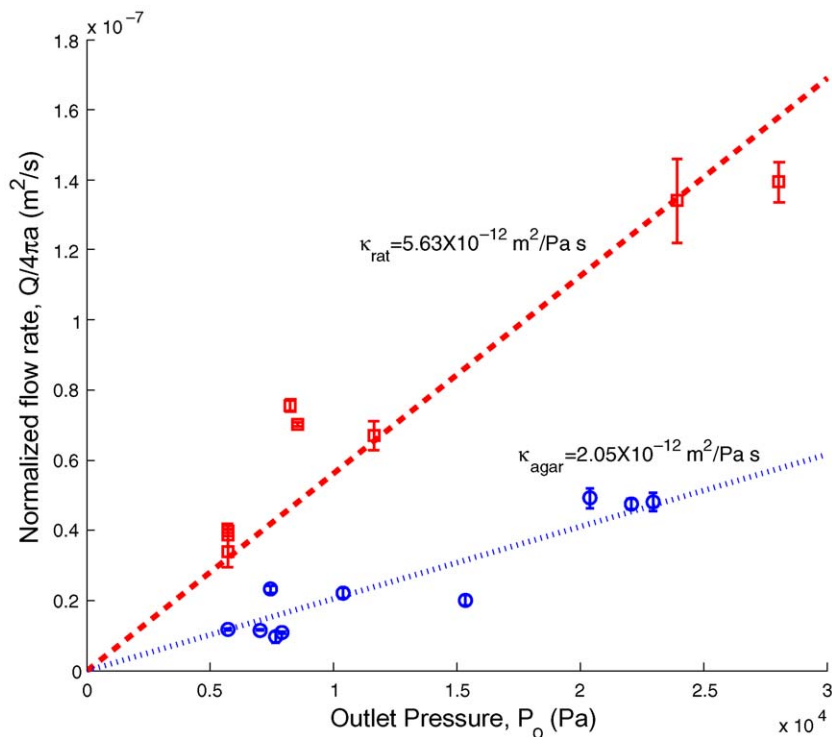
Fig. 3. The apparent hydraulic permeability was calculated using Darcy's Law in radial coordinates, where $P_o = (Q(a)/4\pi a)\kappa$, for injection into 0.6% agarose (O) or brain (□). The x-axis is the pressure at the tip of the device. The injector pressure upstream from the device was 7–210 kPa. The flow rate was estimated by measuring the time it took for 1 μL of volume to be expelled through the device into the gel or tissue. Each symbol represents one infusion. There were 5–20 measurements taken for each infusion depending on the infused volume and the error bars represent one standard deviation from these measurements. Best fits of Eq. (8) to experimental data are shown by dashed lines.

experiment, $Q$ was measured and this formula was used to find $\Delta P$, which was then subtracted from the injector pressure to determine the pressure at the channel outlet, $P_o$.

### 3.2. Distributions of infused compounds and backflow

The infusion of dye into agarose gels was studied for injector pressures of 7, 35, 70, 140, 210, and 310 kPa, which corresponded to infusion flow rates of 0.08, 0.4, 0.8, 1.7, 2.9, 4.5 μL/min, respectively. In every case, the infusions resulted in spherically symmetric dye distributions about the exit of the microchannel. There was no visual evidence of backflow at any of these injector pressures. Fig. 3 shows a linear relationship between $Q(a) = 4\pi a$ and $P_o$; according to Eq. (8), the slope of this line gives an apparent hydraulic conductivity for 0.6% agarose of $2.05 \times 10^{-12}$ m²/Pa s. Even at the lowest injector pressure (7 kPa),
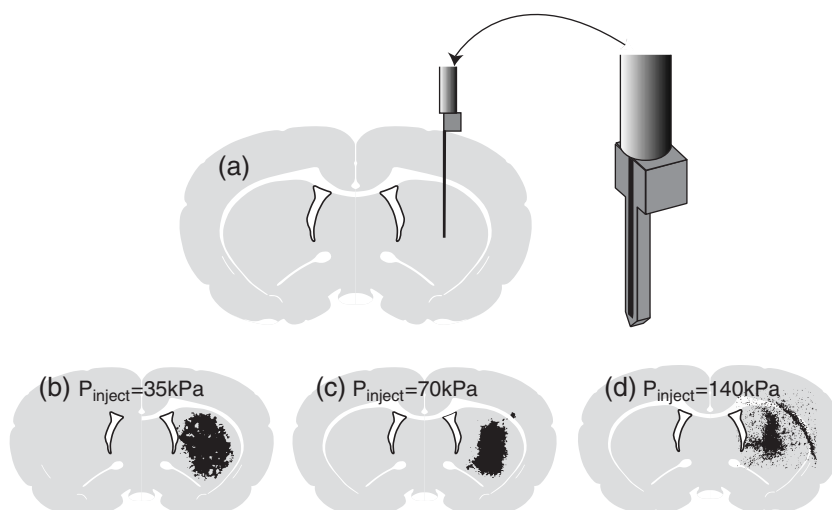


Fig. 4. (a) The microfluidic probe with attached fluid reservoir was inserted 3 mm laterally from bregma to a depth of 5 mm into the caudate nucleus (Top). (b)–(d)An overlay of the processed data on a cartoon of the insertion site illustrates the pressure dependence of the dye distribution at injection pressure of 35, 70, and 140 kPa. Adapted from Retterer et al. [30].
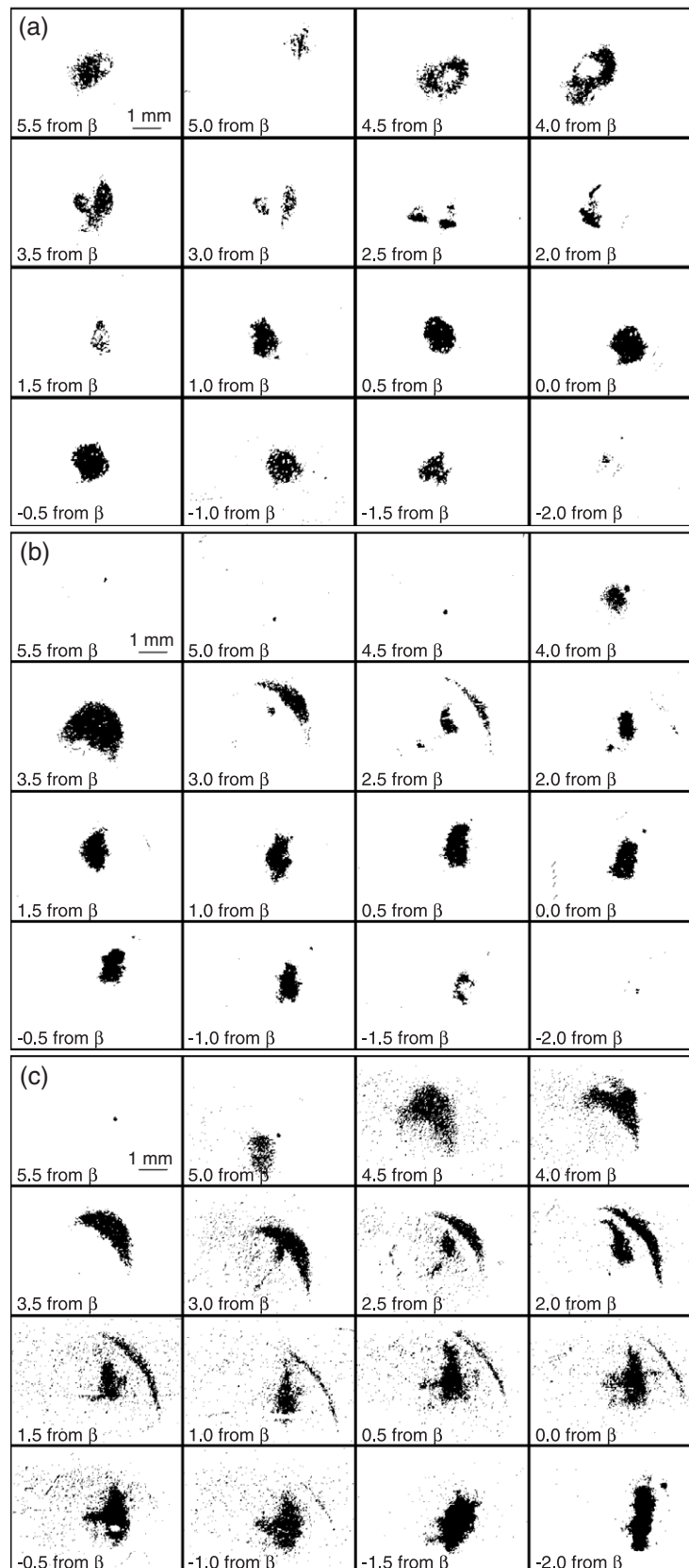
Fig. 5. Distribution of Evans blue labeled albumin in the caudate of rats at infusion pressures of (a) 35, (b) 70, and (c) 140 kPa. Each coronal slice is labeled by its position with respect to bregma ($\beta$) in millimeters. The infusion site is at 0.0 mm from bregma.

penetration of the dye was observed immediately, suggesting that the probe outlet was not occluded. There was no evidence of a pressure barrier to initiate flow. In contrast, for infusion through a blunt 30 ga needle inserted into the gel in the same manner, the pressure had to exceed 11 kPa before there was evidence of flow. To compare the performance of the microfabricated device with that of a needle, the injector pressure was increased in stages until the onset of backflow was observed. For the microfluidic device at an insertion depth of 5 mm, the backflow was observed when pressure was increased to $310 \pm 8$ kPa ($n = 10$) corresponding to a flow rate of 4.5 µL/min. For a 30 ga needle backflow was observed when the pressure was increased to 20 kPa$\pm 4$ ($n = 10$) corresponding to a flow rate of 0.41 µL/min.

The device was inserted 3 mm laterally from bregma into the caudate of the rates to a depth of 5 mm (Fig. 4(a)). The infusion of dye was studied for injector pressures of 35, 70, and 140 kPa (Fig. 4(b–d)). In these cases the infusions resulted in dye distributions that were nearly elliptical except in one case at 140 kPa (Fig. 4(d)). Fig. 3 shows that the relationship between flow rate and pressure at the outlet of the channel, $P_o$, was linear, and a comparison of data with Eq. (8) yielded a value of $5.63 \times 10^{-12}$ m$^2$/Pa s for the apparent hydraulic permeability of gray matter in the caudate putamen.

The shapes of the dye distributions in the rat brain depended on the injector pressure. Fig. 5 shows processed images of the dye distributions for the three values of the injector pressure. Each montage contains coronal slices from a single brain at a given pressure. The slices are separated by 0.5 mm. Their distances from bregma are given in millimeters; positive numbers refer to the slices anterior to bregma and negative numbers refer to slices posterior to bregma.

At an injector pressure of 35 kPa, the distribution of dye within each coronal section was slightly non-spherical (Figs. 4(b) and 5(a)). At 70 (Figs. 4(c) and 5(b)) and 140 kPa (Figs. 4(d) and 5(c)) the distributions were more elongated. Single factor analysis of the variance (ANOVA) was performed on both the total volume of dye in the gray matter and the aspect ratio of the distribution at the infusion site (3 mm lateral from bregma). Tables 1 and 2 show a summary of the ANOVA results for an alpha value of 0.05 for volume and aspect ratio, respectively. In both cases there were statistically significant ($p < 0.05$) differences between the low, medium, and high pressure groups. However, there was not a statistically significant difference in the aspect ratio beyond the infusion site. This result suggests

Table 1

Analysis for the variance of volume of dye in the gray matter between low (35 kPa), medium (70 kPa), and high (140 kPa) injector pressures

| Groups | Count | Sum | Average | Variance |
|---|---|---|---|---|
| Low pressure | 3 | 7.6 | 2.5 | 0.11 |
| Medium pressure | 3 | 8.3 | 2.8 | 0.17 |
| High pressure | 3 | 11.4 | 3.8 | 0.01 |

| Source of variation | SS | df | MS | F | P-value | F crit |
|---|---|---|---|---|---|---|
| Between groups | 3.5 | 2 | 1.8 | 18 | 0.02 | 9.6 |
| Within groups | 0.3 | 6 | 0.10 | | | |
| Total | 3.8 | 8 | | | | |

Table 2

Analysis for the variance of the aspect ratio at 0 mm from bregma between low (35 kPa), medium (70 kPa), and high (140 kPa) injector pressures

| Groups | Count | Sum | Average | Variance |
|---|---|---|---|---|
| Low pressure | 3 | 3.6 | 1.2 | 0.004 |
| Medium pressure | 3 | 4.91 | 1.6 | 0.068 |
| High pressure | 3 | 4 | 1.3 | 0.002 |

| Source of variation | SS | df | MS | F | P-value | F crit |
|---|---|---|---|---|---|---|
| Between groups | 0.32 | 2 | 0.16 | 6.4 | 0.03 | 5.1 |
| Within groups | 0.15 | 6 | 0.025 | | | |
| Total | 0.47 | 8 | | | | |

that asymmetrical distribution was limited to tissue immediately adjacent to the device.

Evidence of backflow was found in one of three cases for an injection pressure of 140 kPa but in no cases for 35 or 70 kPa. The crescent-shaped distributions in Fig. 5(c) are indicative of backflow. In this case, the infused dye migrated into the white matter of the corpus callosum immediately above the caudate as a result of backflow along the outside of the microchannel. Once in the white matter, the dye then flowed in anterior and posterior directions. Backflow in this case may have been caused by a poor insertion, which can increase the likelihood of backflow [30]. During curing of the epoxy, occasionally the device becomes slightly misaligned with the micropipette that holds it. In this event the device is not exactly perpendicular to the surface as it is inserted, which can lead to tissue tearing and backflow.

Owing to the small size of the rat brain, dye reached white matter even in the absence of backflow. The caudate putamen is the largest area of homogeneous gray matter. It is roughly spherical with a diameter of approximately 3.0 mm and is surrounded by a white matter envelope consisting of the corpus callosum [46]. Infused albumin reached the anterior forceps of the corpus callosum at a penetration distance of 2 mm and subsequently flowed several millimeters in the anterior direction. This projection is clearly seen in Fig. 5(b) which shows dye up to 4 mm anterior to the infusion site. Such extensive penetration is unlikely in gray matter, but it could occur by transport through the high permeability tracts of white matter.

### 3.3. The effect of diffusion on penetration distance

The potential advantage of CED is that penetration into tissue can be enhanced by convection compared with the penetration obtained by diffusion in controlled release. Convection dominates diffusion near the microchannel tip, but the infusion velocity decays as $1/r^2$ where $r$ is the distance from the tip. If the infused drug penetrates sufficiently far from the infusion point, then its transport may be dominated by diffusion at its farthest penetration. The distance where this occurs depends not only on the infusion rate, but also on the diffusivity of the injected molecules.

To show how diffusion can affect the penetration distance in CED, infusions into agarose were compared for two infused
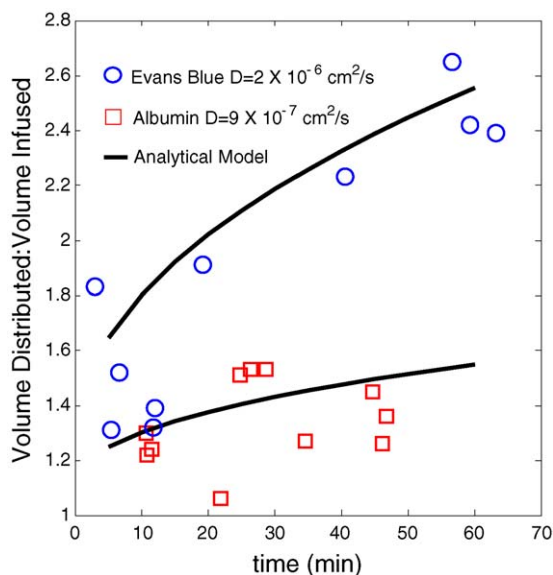
Fig. 6. Volume distributed : volume infused of Evans Blue (○) and albumin (□) into 0.6% agarose at an infusion pressure of 5 kPa and a comparison to model predictions (–). Each data point represents a separate infusion. The model accurately predicts the time dependent $V_d$ : $V_i$ observed with infusion of Evans Blue ($R^2 = 0.70$) compared to the relatively time insensitive results obtained during infusion of albumin ($R^2 = 0.83$).

molecules: a small water soluble molecule (Evans Blue) and a large globular protein (albumin). Infusions of various durations were performed and the volume of gel containing dye $V_d$ was measured and compared with the known volume of fluid $V_i$ that was infused. Fig. 6 shows the ratio $V_d / V_i$ as a function of infusion time. In the absence of diffusion, corresponding to an infinitely large Peclet number everywhere throughout the flow, the ratio $V_d / V_i$ would equal the inverse of the porosity $1 / \phi$ regardless of the infusion time. However, the data show that the ratio depends on infusion time, which indicates that diffusion affects the penetration distance. The ratio is larger and shows greater sensitivity to infusion time for Evans Blue, which is expected from Eq. (11) based on its larger diffusivity ($D = 2.0 \times 10^{-6}$ cm$^2$/s, Stokes–Einstein equation, molecular radius from Markou et al. [47]) compared with the diffusivity of albumin ($D = 8.3 \times 10^{-7}$ cm$^2$/s in 0.3% agarose [48]). Data for both compounds were compared with the model described in Section 2.6 by using Eq. (11) to estimate the penetration depth for the appropriate experimental parameters. The result shown in Fig. 6 shows good agreement between the model and the data over a wide range of infusion times. The coefficient of multiple determination ($R^2$) was 0.70 for Evans Blue and 0.83 for albumin.

## 4. Discussion

The microfabricated devices described here have several advantages over larger needles for CED. The devices can deliver liquids at flow rates comparable to those in CED with needles with reduced backflow that often hampers fluid delivery through needles [27,26]. In principle, devices can be fabricated for specific anatomical geometries with the option of placing

several delivery outlets on a single device. In addition, other components can be incorporated into microfabricated devices, including recording/stimulating electrodes, pumps, valves, and flow meters.

Infusing at constant pressure rather than at constant flow rate has important consequences on the pressure and stress distributions in the tissue. For constant pressure infusion, the pressure profile in the tissue is independent of the tissue's material properties (Eq. (6)), including its hydraulic permeability. Furthermore, Netti et al. showed that for constant pressure infusion into a poroviscoelastic material, the radial and circumferential stress components also are independent of the hydraulic permeability [44]. In contrast, the pressure and stress components are strongly affected by the hydraulic permeability for constant flow rate infusion. If sufficiently high levels of stress incite apoptotic or necrotic signalling cascades in neurons or glial cells [49], then knowing the stress profile even when the hydraulic permeability is uncertain is an advantage of constant pressure infusion.

There is a wide range of values reported for hydraulic permeability in tissues and gels (from $1 \times 10^{-11}$ to $1 \times 10^{-16}$ m$^2$/Pa s) [22,50,42,49,44]. Our value of $2.05 \times 10^{-12}$ m$^2$/Pa s for gray matter in the rat agrees reasonably well with Basser's estimate of $5 \times 10^{-12}$ m$^2$/Pa s [42]. However, the permeability of elastic or viscoelastic porous media depends on deformation of the media. For example, Deen and Johnson show that the permeability of agarose decreases in uniaxial flow owing to compression of the void space in the gel [50]. In a radial source flow like the one presented here, the magnitudes and signs of the radial and circumferential stress components determine whether the tissue is dominated by compression or tension. Zhang et al. found an increase in permeability with respect to infusion pressure in radial flow in fibrosarcomas under constant pressure infusion (2–16 kPa) of albumin [51]. For constant pressure infusion with our microfluidic probes, the apparent hydraulic permeability did not depend on flow rate in agarose or in brain tissue. However, the apparent hydraulic permeability is calculated based on the pressure and flow rate at one point, the infusion site. To distinguish local permeability changes in response to flow, one would need to measure pressure as a function of distance [22].

The apparent value we report may overestimate the actual permeability of a poroelastic medium since dilation is expected to be greatest at the infusion site, leading to increased porosity and higher permeability there.

Several investigators have observed an increase in pressure followed by a precipitous decrease to a steady-state value at the beginning of constant flow rate infusions. This result has been attributed to the elasticity of brain tissue [27], the opening of fluid channels in the extracellular matrix [51], and simply occlusion of the needle tip [4]. Our observations are consistent with the last explanation. During constant pressure infusion into 0.6% agarose using a blunt needle we found that a critical pressure (~10 kPa) was necessary to observe convective flow. When the pressure was increased to values only slightly larger than this critical pressure, a burst of dye was suddenly infused followed by significant backflow at insertion depths of 5 mm. The microfluidic devices did not exhibit any pressure increases

during infusion. Infusion is observed immediately at the start, regardless of injector pressure.

The size of the delivery device for CED affects the maximum allowable infusion rate without backflow for a given insertion depth. A previous study of infusions of 4 µL of albumin through a 32 ga needle (OD=0.228 mm) into the caudate of rats showed that the maximum flow rate without backflow into the corpus callosum was 0.5 µL/min [25]. Lonser et al. infused the brainstem of primates with a 32 ga needle at flow rates of 0.25–1 µL/min [9] without backflow. Our microfluidic probes achieved flow rates of 2.0 µL/min (140 kPa injector pressure). In one animal, we found a crescent shape distribution (Fig. 4c) indicative of backflow into the corpus callosum. However, backflow in this case was most likely due to a poor insertion.

Using scaling arguments, Morrison et al. found $x_m =$ constant$Q^{0.6}r_c^{0.8}$, where $x_m$ is the axial length of backflow, $Q$ is the flow rate, $r_c$ is the catheter radius, and the constant is related to the physical properties of the porous medium [26]. For infusions into the gray matter of rats they found $x_m(\text{cm}) = 11.41Q$ $(\mu\text{L/min})^{0.6}r_c(\text{cm})^{0.8}$. Applying this formula to the microfluidic probes using a hydraulic radius of 0.05 mm ($r_c$=area/(perimeter/2)) gives a maximum flow rate of 1.6 µL/min which is similar to our observations.

Human clinical trials for the treatment of malignant gliomas with off-the-shelf catheters have shown promise in treating tumors and resection cavities [24]. The large size of the targeted tumors (~1–5 cm) and kinetics of the cytotoxic agents require long infusion times (2–4 days) and high flow rates (5–10 µL/min). Applying Morrison's scaling relationship for gray matter to these high flow rates with a 32 ga needle gives backflow distances of one to 2 cm. A microfluidic device could be designed using the process described in this study to have a hydraulic radius as small as 10 µm. If the scalings hold down to this size, such a device would result in backflow distances of only a few millimeters even at flow rates up to 10 µL/min.

## 5. Conclusions

Microfluidic devices have been fabricated that are capable of delivering liquids at relevant flow rates for convection enhanced drug delivery. The small size and geometry of these devices offer potential advantages over traditional needle/catheter infusion protocols. The orientation of the channel inlets on the top of the device inhibits channel occlusion during insertion into tissue. The use of a small channel operating under constant pressure infusion leads to stress fields that are local (~100 µm) and independent of hydraulic permeability which helps minimize backflow and produce spherical distributions of infused fluids, at least in porous media. Fluid distribution into the caudate of rats showed slight asymmetry. In direct comparison with needles in agarose brain phantoms, microfluidic devices could operate at ten times the flow rate before inducing backflow out of the brain phantom at a 5 mm insertion depth. Similarly, in vivo infusions into the caudate of rats were tolerated at flow rates four times higher than those previously reported.

## References

[1] C.E. Krewson, M.L. Klarman, W.M. Saltzman, Distribution of nerve growth-factor following direct delivery to brain interstitium, Brain Res. 680 (1–2) (1995) 196–206.

[2] L.K. Fung, M.G. Ewend, A. Sills, E.P. Sipos, R. Thompson, M. Watts, O.M. Colvin, H. Brem, W.M. Saltzman, Pharmacokinetics of interstitial delivery of carmustine, 4-hydroperoxycyclophosphamide, and paclitaxel from a biodegradable polymer implant in the monkey brain, Cancer Res. 58 (4) (1998) 672–684.

[3] W.M. Saltzman, M.L. Radomsky, Drugs released from polymers: diffusion and elimination in brain tissue, Chem. Eng. Sci. 46 (10) (1991) 2429–2444.

[4] R.H. Bobo, D.W. Laske, A. Akbasak, P.F. Morrison, R.L. Dedrick, E.H. Oldfield, Convection-enhanced delivery of macromolecules in the brain, Proc. Natl. Acad. Sci. U. S. A. 91 (6) (1994) 2076–2080.

[5] R.R. Lonser, M.E. Corthésy, P.F. Morrison, N. Gogate, E.H. Oldfield, Convection-enhanced selective excitotoxic ablation of the neurons of the globus pallidus internus for treatment of parkinsonism in nonhuman primates, J. Neurosurg. 91 (1999) 294–302.

[6] D.R. Groothuis, S. Ward, A.C. Itskovich, C. Dobrescu, C.V. Allen, C. Dills, R.M. Levy, Comparison of c-14-sucrose delivery to the brain by intravenous, intraventricular, and convection-enhanced intracerebral infusion, J. Neurosurg. 90 (2) (1999) 321–331.

[7] D.M. Lieberman, D.W. Laske, P.F. Morrison, K.S. Bankiewicz, E.H. Oldfield, Convection-enhanced distribution of large molecules in gray-matter during interstitial drug infusion, J. Neurosurg. 82 (6) (1995) 1021–1029.

[8] D.W. Laske, P.F. Morrison, D.M. Lieberman, M.E. Corthesy, J.C. Reynolds, P.A. Stewart-Henney, S.S.K.A. Cummins, C.H. Paik, E.H. Oldfield, Chronic interstitial infusion of protein to primate brain: determination of drug distribution and clearance with single-photon emission computerized tomography imaging, J. Neurosurg. 87 (1997) 586–594.

[9] R.R. Lonser, S. Walbridge, K. Garmestani, J.A. Butman, H.A. Walters, A.O. Vortmeyer, P.F. Morrison, M.W. Brechiel, E.H. Oldfield, Successful and safe perfusion of the primate brainstem: in vivo magnetic resonance imaging of macromolecular distribution during infusion, J. Neurosurg. 97 (2002) 905–913.

[10] J.F. Hamilton, P.F. Morrison, M.Y. Chen, J. Harvey-White, R.S. Pernaute, H. Phillips, E. Oldfield, K.S. Bankiewiczl, Heparin coinfusion during convection-enhanced delivery (ced) increases the distribution of the glial-derived neurotrophic factor (gdnf) ligand family in rat striatum and enhances the pharmacological activity of neurturin, Exp. Neurol. 168 (2001) 155–161.

[11] W. Yang, R.F. Barth, D.M. Adams, M.J. Ciesielski, R.A. Fenstermaker, S. Shukla, W. Tjarks, M.A. Cligiuri, Convection-enhanced delivery of boronated epidermal growth factor for molecular targeting of egf receptor-positive gliomas, Cancer Res. 62 (2002) 6552–6558.

[12] W.C. Broaddus, S.S. Prabhu, G.T. Gillies, J. Neal, W.S. Conrad, Z. Chen, H. Fillmore, H.F. Young, Distribution and stability of antisense phosphorothioate oligonucleosides in rodent brain following direct intraparenchymal controlled-rate infusion, J. Neurosurg. 88 (1998) 734–742.

[13] D.R. Groothuis, H. Benalcazar, C.V. Allen, R.M. Wise, C. Dills, C. Dobrescu, V. Rothholtz, R.M. Levy, Comparison of cytosine arabinoside delivery to rat brain by intravenous, intrathecal, intraventricular and

intraparenchymal routes of administration, Brain Res. 856 (1–2) (2000) 281–290.

[14] Y. Mardor, Y. Roth, Z. Lidar, T. Jonas, R. Pfeffer, S.E. Maier, M. Faibel, D. Nass, M. Hadani, A. Orenstein, J.S. Cohen, Z. Ram, Monitoring response to convection-enhanced taxol delivery in brain tumor patients using diffusion-weighted magnetic resonance imaging, Cancer Res. 61 (2001) 4971–4973.

[15] Z. Lidar, Y. Mardor, T. Jonas, R. Pfeffer, M. Faibel, D. Nass, M. Hadani, Z. Ram, Convection-enhanced delivery of paclitaxel for the treatment of recurrent malignant glioma: a phase i/ii clinical study, J. Neurosurg. 100 (2004) 472–479.

[16] H. Ren, T. Boulikas, A. Söling, P.C. Warnke, N.G. Rainov, Immunogene therapy of recurrent glioblastoma multiforme with a liposomally encapsulated replication-incompetent semliki forest virus vector carrying the human interleukin-12 gene a phase i/ii clinical protocol, J. Neurooncol. 64 (2003) 147–154.

[17] J.H. Sampson, G. Akabani, G.E. Archer, D.D. Bigner, M.S. Berger, A.H. Friedman, H.S. Friedman, J. Herndon II, S. Kunwar, S. Marcus, R.E. McLendon, A. Paolino, K. Penne, J. Provenzale, J. Quinn, D.A. Reardon, J. Rich, T. Stenzel, S. Tourt-Uhlig, C. Wikstrand, T. Wong, R. Williams, F. Yuan, M.R. Zalutsky, I. Pastan, Progress report of a phase i study of the intracerebral microinfusion of a recombinant chimeric protein composed of transforming growth factor (tgf)-α and a mutated form of the *Pseudomonas* exotoxin termed pe-38 (tp-38) for the treatment of malignant brain tumors, J. Neuro-oncol. 65 (2003) 27–35.

[18] F. Weber, A. Asher, R. Bucholz, M. Berger, M. Prados, S. Chang, J. Bruce, W. Hall, N.G. Rainov, M. Westphal, R.E. Warnick, R.W. Rand, F. Floeth, F. Rommel, H. Pan, V.N. Hingorani, R.K. Puri, Safety, tolerability, and tumor response of il4-*Pseudomonas* exotoxin (nbi-3001) in patients with recurrent malignant glioma, J. Neuro-oncol. 64 (2003) 125–137.

[19] J.K. Ratliff, E.H. Oldfield, Convection-enhanced delivery in intact and lesioned peripheral nerve, J. Neurosurg. 95 (2001) 1001–1011.

[20] D.I. Sandberg, M.A. Edgar, M.M. Souweidane, Convection-enhanced delivery into the rat brainstem, J. Neurosurg. 96 (2002) 885–891.

[21] G. Occhiogrosso, M.A. Edgar, D.I. Sandberg, M.M. Souweidane, Prolonged convection-enhanced delivery into the rat brainstem, Neurosurgery 52 (2) (2003) 388–393.

[22] Y. Boucher, C. Brekken, P.A. Netti, L.T. Baxter, R.K. Jain, Intratumoral infusion of fluid: estimation of hydraulic conductivity and implications for the delivery of therapeutic agents, Br. J. Cancer 78 (11) (1998) 1442–1448.

[23] T.T. Nguyen, Y.S. Pannu, C. Sung, R.L. Dedrick, S. Walbridge, M.W. Brechbiel, K. Garmestani, M. Beitzel, A.T. Yordanov, E.H. Oldfield, Convective distribution of macromolecules in the primate brain demonstrated using computerized tomography and magnetic resonance imaging, J. Neurosurg. 98 (2003) 584–590.

[24] M.A. Vogelbaum, Convection enhanced delivery for the treatment of malignant gliomas: symposium review, J. Neuro-oncol. 73 (2005) 57–69.

[25] M.Y. Chen, R.R. Lonser, P.F. Morrison, L.S. Governale, E.H. Oldfield, Variables affecting convection-enhanced delivery to the striatum: a systematic examination of rate of infusion, cannula size, infusate concentration, and tissue–cannula sealing time, J. Neurosurg. 90 (2) (1999) 315–320.

[26] P.F. Morrison, M.Y. Chen, R.S. Chadwick, R.R. Lonser, E.H. Oldfield, Focal delivery during direct infusion to brain: role of flow rate, catheter diameter, and tissue mechanics, Am. J. Physiol. Regul. Integr. Comp. Physiol. 277 (4) (1999) R1218–R1229.

[27] Z. Chen, G.T. Gillies, W.C. Broaddus, S.S. Prabhu, H. Fillmore, R.M. Mitchell, F.D. Corwin, P.P. Fatouros, A realistic brain tissue phantom for intraparenchymal infusion studies, J. Neurosurg. 101 (2004) 314–322.

[28] J.D. Zahn, N.H. Talbot, D. Liepmann, A.P. Pisano, Microfabricated polysilicon microneedles for minimally invasive biomedical devices, Biomed. Microdevices 2 (4) (2000) 295–303.

[29] J.K. Chen, K.D. Wise, J.F. Hetke, S.C. Bledsoe, A multichannel neural probe for selective chemical delivery at the cellular level, IEEE Trans. Biomed. Eng. 44 (8) (1997) 760–769.

[30] S.T. Retterer, K.L. Smith, C.S. Bjornsson, K.B. Neeves, A.J. Spence, J.N. Turner, W. Shain, M.S. Isaacson, Model neural prostheses with integrated microfluidics: a potential intervention strategy for controlling reactive cell and tissue responses, IEEE Trans. Biomed. Eng. 51 (11) (2004) 2063–2073.

[31] R. Rathnasingham, D.R. Kipke, S.C. Bledsoe Jr., J.D. McLaren, Characterization of implantable microfabricated fluid delivery devices, IEEE Trans. Biomed. Eng. 51 (1) (2004) 138–145.

[32] D. Papageorgiou, S.C. Bledsoe, M. Gulari, J.F. Hetke, D.J. Anderson, K.D. Wise, A shuttered probe with in-line flowmeters for chronic in vivo drug delivery, Proc. 14th IEEE Int. Conf. Micro Electro Mechanical Systems Conf., 2001, pp. 212–215.

[33] J.D. Zahn, A. Deshmukh, A.P. Pisano, D. Liepmann, Continuous on-chip micropumping for microneedle enhanced drug delivery, Biomed. Microdevices 6 (2004) 183–190.

[34] A.B. Schwartz, Cortical neural prosthetics, Annu. Rev. Neurosci. 27 (2004) 487–507.

[35] D.R. Kipke, R.J. Vetter, J.C. Williams, J.F. Hetke, Silicon-substrate intracortical microelectrode arrays for long-term recording of neuronal spike activity in cerebral cortex, IEEE Trans. Neural Syst. Rehabil. Eng. 11 (2003) 151–155.

[36] H.F. Cserr, L.H. Ostrach, Bulk flow of interstitial fluid after intracranial injection of blue dextran 2000, Exp. Neurol. 45 (1974) 50–60.

[37] F. Peña, R. Tapia, Seizures and neurodegenerataion induced by 4-aminopyridine in rat hippocampus in vivo: role of glutamate- and gaba-mediated neurotransmission and of ion channels, Neuroscience 101 (2000) 547–561.

[38] H.E. Sharfman, J.H. Goodman, A.L. Sollas, S.D. Croll, Spontaneous limbic seizures after intrahippocampal infusion of brain-derived neurotrophic factor, Exp. Neurol. 174 (2002) 201–214.

[39] I.A. Yun, K.T. Wakabayashi, H.L. Fields, S.M. Nicola, The ventral tegmental area is required for the behavioral and nucleus accumbens neuronal firing responses to incentive cues, J. Neurosci. 24 (2004) 2923–2933.

[40] P.F. Morrison, D.W. Laske, H. Bobo, E.H. Oldfield, R.L. Dedrick, High-flow microinfusion: tissue penetration and pharmacodynamics, Am. J. Physiol. Regul. Integr. Comp. Physiol. 266 (1994) R292–R305.

[41] L.T. Baxter, R.K. Jain, Transport of fluid and macromolecules in tumors: I. role of interstitial pressure and convection, Microvasc. Res. 37 (1989) 77–104.

[42] P.J. Basser, Interstitial pressure, volume, and flow during infusion into brain tissue, Microvasc. Res. 44 (1992) 143–165.

[43] P.A. Netti, L.T. Baxter, Y. Boucher, R. Skalak, R.K. Jain, Macro- and microscopic fluid transport in living tissues: application to solid tumors, AIChE J. 43 (3) (1997) 818–834.

[44] P.A. Netti, F. Travascio, R.K. Jain, Coupled macromolecular transport and gel mechanics: poroviscoelastic approach, AIChE J. 49 (6) (2003) 1580–1596.

[45] O. Levenspiel, Chemical Reaction Engineering, 3rd Edition, John Wiley and Sons, 1999.

[46] L.W. Swanson, Brain Maps: Structure of the Rat Brain, 2nd Edition, Elsevier, 1998.

[47] C.P. Markou, E.M. Lutostansky, D.N. Ku, S.R. Hanson, A novel method for efficient drug delivery, Ann. Biomed. Eng. 26 (1998) 502–511.

[48] L. Tao, C. Nicholson, Diffusion of albumins in rat cortical slices and relevance to volume transmission, Neuroscience 75 (1996) 839–847.

[49] B.M. III, J.H. Eberwine, D.F. Meaney, T.K. Mcintosh, Traumatic injury induces differential expression of cell death genes in organotypic brain slice cultures determined by complementary DNA array hybridization, Neuroscience 96 (2000) 131–139.

[50] E.M. Johnson, W.M. Deen, Hydraulic permeability of agarose gels, AIChE J. 42 (1996) 1220–1224.

[51] X. Zhang, J. Luck, M.W. Dewhirst, F. Yuan, Interstitial hydraulic conductivity in a fibrosarcoma, Am. J. Physiol. Heart Circ. Physiol. 279 (2000) H2726–H2734.